IVYSPRING INTERNATIONAL PUBLISHER

Nanotheranostics

2018; 2(3): 243-257. doi: 10.7150/ntno.25901

Research Paper

Nd^{3+} sensitized core-shell-shell nanocomposites loaded with IR806 dye for photothermal therapy and up-conversion luminescence imaging by a single wavelength NIR light irradiation

Syue-Liang Lin[1], Zi-Rong Chen[1], C. Allen Chang[1,2,3,✉]

1. Department of Biotechnology and Laboratory Science in Medicine, National Yang-Ming University, Taipei 112, Taiwan.
2. Department of Biomedical Imaging and Radiological Sciences, National Yang-Ming University, Taipei 112, Taiwan.
3. Molecular Imaging Research Center (MIRC), National Yang-Ming University, Taipei 112, Taiwan.

✉ Corresponding author: cachang@ym.edu.tw

Received: 2018.03.09; Accepted: 2018.05.09; Published: 2018.05.24

Abstract

To perform photothermal therapy (PTT) and luminescence imaging by a single wavelength NIR light irradiation, we have designed and prepared a novel nanocomposite incorporating the IR806 photothermal sensitizers (PTS) into the core-shell-shell $NaYF_4$:Yb,Er@ $NaYF_4$:Yb@$NaYF_4$:Yb,Nd up-conversion nanoparticles (UCNPs). Irradiation with the 793 nm near-infrared (NIR) laser, the Nd^{3+} ions in the UCNPs were sensitized to up-convert energy *via* Yb^{3+} to the Er^{3+} ions to emit visible light at 540 nm and 654 nm, as well as to down-convert energy to the Yb^{3+} ions to emit NIR light at 980 nm. For luminescence imaging, the 793 nm NIR radiation is more suitable to use for deeper-tissue penetration and to reduce overheating problem due to water absorption as compared to 980 nm radiation. Additionally, the same 793 nm NIR radiation could also excite the IR806 dye for effective PTT. Surface modifications of the UCNPs with mesoporous silica ($mSiO_2$) and polyallylamine (PAH) allow stable loading of IR806 dye and further derivatization with polyethylene glycol-folic acid (PEG-FA) for tumor targeting. Preliminary *in vitro* studies demonstrated that the final UCNP@$mSiO_2$/IR806@PAH-PEG-FA nanocomposites (UCNC-FAs) could be uptaken by the MDA-MB-231 cancer cells and were "dark" viable, and when irradiated with the 793 nm laser, the MDA-MB-231 cell viability was effectively reduced. This indicated that the UCNC-FAs nanocomposites could be potentially useful for targeted photothermal therapy and up-conversion luminescence imaging by a single wavelength NIR light irradiation.

Key words: Lanthanide, Theranositcs, Photothermal therapy, Nd^{3+} sensitized up-conversion, Near-IR, Luminescence imaging

Introduction

The treatment of cancer may be different depending on the cancer stages and tumor locations, and traditionally, surgery, chemotherapy and radiation therapy are the most common ways[1]. However, these treatments are either invasive or with many side effects or sometime ineffective, e.g. cell toxicity and drug-resistance of chemotherapy as well as problems of overdose, cancer cell mutation and decreasing effectiveness with increasing number of treatments due to radiation therapy. Thus, alternative and adjuvant therapies are currently under clinical development, including immuno-cell therapy[2], targeted chemotherapy[3], photodynamic therapy (PDT)[4] and thermotherapy (or hyperthermia)[5, 6]. The goals are to make cancer therapy to be more specific, theranostic and with low side effects and high precision.

Clinically, thermotherapy[6] coupled with chemotherapy and/or radiation therapy could increase cancer patient survival rate and improve the

control of local lesions. Among the various thermotherapeutic methods, interstitial hyperthermia[7], hyperthermic chemoperfusion[8], and whole-body hyperthermia[9] all increase the temperature of the tumor tissue to about 42°C to induce cell apoptosis. However, these methods lack specificity and often make normal tissues overheated. The long treatment duration also causes the patients uncomfortable and requires anesthesia[10], making thermotherapy less effective and inconvenient. To overcome these problems, the use of nanoparticles has been proposed as the carriers or drugs for targeted thermotherapy[11]. For example, folate modified superparamagnetic iron oxide nanoparticles (SPIOs) in variable-frequency magnetic field could be used to generate heat for targeted thermotherapy *via* intravenous injection. However, because the concentrations of SPIOs at the tumor sites were usually not high enough and the heat conversion efficiency was low, this material could not raise the tumor site temperature to the range for effective thermotherapy[12]. Another example is the photothermal therapy (PTT) employing nanoparticles that could absorb high-tissue-penetrating near infrared (NIR) light with high heat-generation efficiency such as gold nanorod[13]. After surface modification with targeted molecules, they could be delivered to the tumor sites and raised the temperature to 42°C *via* NIR radiation to induce cell apoptosis[14-18]. Other attempts for PTT included the use of the inorganic single-walled carbon nanotubes(SWNTs)[19, 20], graphene[21, 22] and CuS nanodots[23, 24] in addition to the NIR organic dyes indocyanine green (ICG)[25, 26] and the lipophilic heptamethine dye, IR780 iodide[5, 27].

The use of the above-mentioned novel nanomaterials for PTT needs to use diagnostic modalities such as computed tomography (CT)[28], positron-emission tomography (PET)[23], magnetic resonance imaging (MRI)[29, 30], photoacoustic imaging (PAI)[31, 32] and other nuclear medicinal technologies[33] to position the tumor site and to follow up on the drug pharmacokinetic behaviors, causing further complexities. Hence, it is proposed that if the photothermal materials could be coupled with optical imaging functions, better theranostics might be prepared and used more conveniently and effectively. However, current luminescence imaging technologies suffer shallow tissue penetration depth[34] and interferences from the luminescence of biomolecules[35]. Because NIR lights in the 650-950 nm wavelength range are less absorbed by biological tissues and are more effective to penetrate into deeper tissues[13, 36], several nanomaterials[37] have recently been studied for use in photodynamic therapy (PDT)[38, 39], drug delivery[40], luminescence imaging and biosensing[41, 42] employing NIR excitation. For example, the $NaLnF_4:Yb^{3+},Er^{3+}$ (Ln = Y or Gd) up-conversion nanoparticles (UCNPs) could emit visible light for luminescence imaging *via* NIR irradiation with very high signal-to-noise ratios[43, 44]. If similar nanomaterials are used together with the NIR organic dye CyTE-777 or IR-825 as photothermal sensitizer[45, 46], concurrent or separate optical excitations at 980 nm on Yb^{3+} for up-conversion imaging and at 808 nm on NIR organic dye for PTT could be performed to avoid the use of different modalities for diagnosis and therapy. Note also, attempts to apply single wavelength of light triggered dual PDT/PTT and imaging become increasingly popular[5, 47-53], including a few nanomaterials such as SWNTs[47], Gold nanorod containing NIR dye (GNR-dye)[48], IR780 NIR dye[5] and core/satellite polydopamine@Nd^{3+} UCNP[51].

It is further noted that water molecules in biological tissues also absorb effectively at 980 nm[54]. Thus, long 980 nm radiation time with high power that exceeds bio-tolerable doses could create local tissue overheating problems[50, 55]. In addition, using two different light wavelengths for diagnosis and therapy could be less convenient than to use a single light wavelength for both purposes. On the other hand, although NIR dyes have high light-absorptivity per mass and are suitable for either tumor luminescence imaging or PTT, they could not be used for both purposes at the same time. This is because high luminescence intensity for imaging requires low dye concentration, and the phenomenon of concentration quenching occurs as the optimum imaging dye concentration is increased much more to achieve better PTT. Thus, if organic dyes are to be used as photothermal sensitizers (PTS), other photosensitizers (PS) such as UCNPs would have to be used for imaging. However, if both type PS are present, there could be competitions between luminescence intensity and photothermal efficiency, and optimization is required.

With the above discussed considerations, to achieve the goals of safety, efficacy and convenience for use in PTT therapy and luminescence imaging, we have designed and prepared an alternative novel nanomaterial, i.e. $NaYF_4:Yb^{3+},Er^{3+}$ @ $NaYF_4:Yb^{3+}$ @ $NaYF_4$: Yb^{3+},Nd^{3+} core-shell-shell UCNPs loaded with the PTS IR806 dye (λ_{max} = 790 nm[56]). This nanocomposite could allow the excitation of the Nd^{3+} ions at 793 nm[54, 57] to increase tissue penetration depth and reduce overheating problem due to water absorption at 980 nm[58], and through internal up-conversion energy transfer from Nd^{3+} *via* Yb^{3+} to

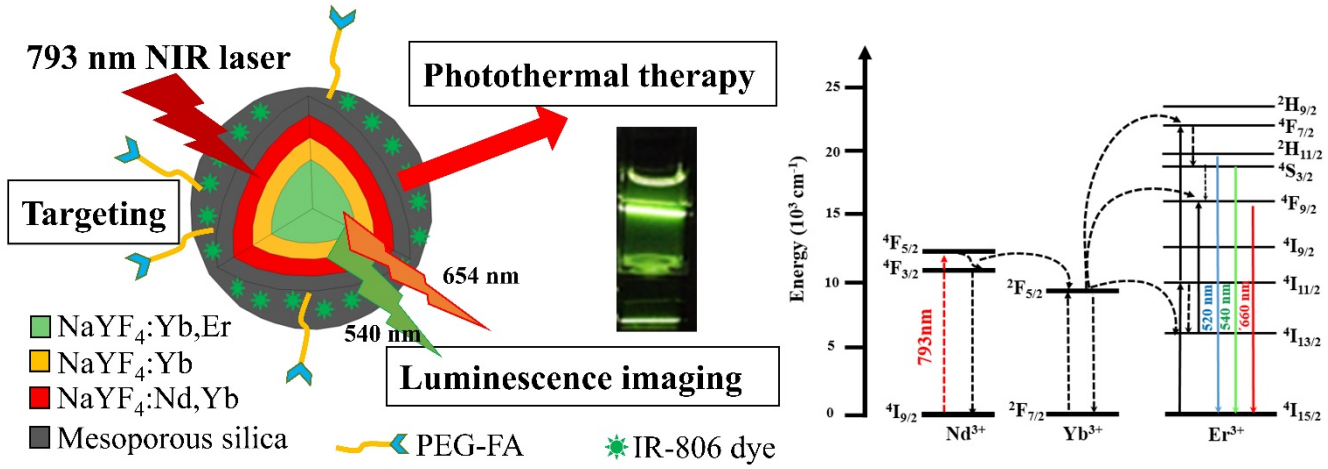

Scheme 1.

Er^{3+} ions to emit lights at 540 nm and 654 nm for diagnostic luminescence imaging. Simultaneously, the IR806 dye could be excited by the same 793 nm irradiation for PTT. The core-shell-shell arrangement[58, 59] could further prevent energy back transfer from Er^{3+} ions to Nd^{3+} ions to preserve light emitting efficiency[55]. If biomarker derivatives such as polyethylene glycol-folic acid (PEG-FA) are attached, the resulting nanocomposites could be used for selective targeted PTT. Scheme 1 shows the representation of this Nd^{3+} ion sensitized novel up-conversion core-shell-shell nanocomposite and relevant simplified energy diagrams of the lanthanide ions. And herein we report our research results.

Experimental Section

Chemicals

Reagent or HPLC grade chemicals used were purchased from Sigma-Aldrich (St Louis, MO, USA): yttrium acetate hydrate, ytterbium acetate hydrate, erbium acetate hydrate, neodymium acetate hydrate, oleic acid, 1-octadecene, sodium hydroxide, ammounium fluoride, ammounium nitrate, ethyl acetate, tetraethyl orthosilicate, chloroform, IR780 iodide, 4-mercaptobenzoic acid, N,N-dimethylformamide, polyallylamine hydrochloride (mw 17000), dimethyl sulfoxide, and cell counting kit 8; from Thermo Fisher Scientific (Waltham, MA, USA): n-hexane, acetone, methanol, and ethanol; from Tokyo Chemical Industry (Tokyo, Japan): n-hexadecyltrimethylammonim chloride (CTAC); from Nanocs (New York, NY, USA): FA-PEG-NHS ester (mw 3400). All chemicals were used as received without further purification.

Characterization

The morphology image measurements of nanoparticles were carried out on a JEM-2000EX II transmission electron microscope (TEM) that operating at an acceleration voltage of 100 kV. High-resolution transmission electron microscope (HR-TEM) images and energy-dispersive X-ray spectroscopy (EDS) data were recorded on a JEOL-JEM 2010F operated at an acceleration voltage of 200 kV. X-ray powder diffraction (XRD) measurements were performed with a Bruker D8 X-ray powder diffractometer (scanning rate: 15°/min, 2θ range: 10° to 80°). Elemental analysis of the lanthanide ion content was determined by using the Agilent 725 inductively coupled plasma optical emission spectrometry (ICP-OES), by the Instrument Center at National Tsing Hua University, Hsinchu, Taiwan. Photoluminescence spectra were recorded with a FSP-920 steady-state and phosphorescence lifetime spectrometer (Edinburgh Instruments) equiped with a 125 mW 793 nm laser. The uv–vis spectra were recorded in 1 cm quartz cuvettes with a Hewlett-Packard/Agilent 8453 diode-array uv–vis spectrophotometer. The size distributions of nanoparticles were determined by SZ-100 zetasizer for dynamic light scattering (DLS) measurement (HORIBA Scientific). HPLC analysis was performed with the instrument equiped with a Waters 1525 pump and a Waters 2489 UV/visible detector (Waters Corp.). NMR spectra were recorded on a Bruker spectrometer Avance III 400 at 400 MHz (^{1}H NMR), 100 MHz (^{13}C NMR). Fluorescence images were performed on an Olympus FV1000-IX81 laser confocal microscope. Digital photo-graphs were taken with a Sony RX100-2 camera. All the nanoparticles under current study were prepared by procedures described below and characterized by similar experimental conditions and instrumentation settings using in-house standard operation procedures (SOPs) including careful calibration.

Synthesis of the core $NaYF_4$:Yb,Er NPs

The lanthanide (Ln)-doped nanoparticles (NPs) were prepared according to a literature reported method with minor modifications[57]. To synthesize the core $NaYF_4$:Yb,Er NPs, a total of 1 mmol $Ln(CH_3COO)_3$ precursors in the Y:Yb:Er = 78:20:2 mol% ratios were mixed in a solution containing 10 mL oleic acid (OA) and 15 mL octadecene (ODE). The mixture was heated to 180 °C under an argon flow for 1 h to result in a homogeneous solution. After cooling to room temperature, 10 mL methanol solution containing 0.15 g NH_4F and 0.1 g NaOH was slowly added to the solution with stirring for 1 h at 65 °C. The temperature of the mixture was then increased to about 100 °C to evaporate the methanol. Subsequently, the solution was heated to 300 °C for 1.5 h and cooled to room temperature. The resulting $NaYF_4$:Yb^{3+}(20%), Er^{3+}(2%) NPs were precipitated, washed by ethanol, collected by centrifugation and redispersed in 15 mL n-hexane. Yield 76 %. Elemental analysis data (ICP, ppm): Y, 13.10; Yb, 6.70; Er, 0.71.

Synthesis of the core-shell $NaYF_4$:Yb,Er@$NaYF_4$:Yb NPs

0.4 mmol $Y(CH_3COO)_3$ and 0.1 mmol $Yb(CH_3COO)_3$ were added to a solution containing 10 mL OA and 15 mL ODE with stirring. The mixture was then heated to 180 °C for 1 h to obtain a homogeneous solution. After the solution was cooled down to room temperature, 7.5 mL of the previously synthesized core $NaYF_4$:Yb,Er NPs in n-hexane was added along with 5 ml methanol containing 0.05 g NH_4F and 0.075 g NaOH. The mixture was stirred for 1 h at 65 °C and heated to 100 °C to evaporate n-hexane and methanol before heating to 300 °C for 1.5 h under argon flow, and then cooled down to room temperature. The resulting core-shell $NaYF_4$:Yb^{3+}(20%), Er^{3+}(2%)@$NaYF_4$:Yb^{3+}(20%) NPs were precipitated, washed with ethanol, collected by centrifugation and redispersed in 15 mL n-hexane. Yield 88 %. Elemental analysis data (ICP, ppm): Y, 17.14; Yb, 9.45; Er, 0.46.

Synthesis of the core-shell-shell $NaYF_4$:Yb,Er@$NaYF_4$:Yb@$NaYF_4$:Yb,Nd UCNPs

Lanthanide precursors of 0.3 mmol $Y(CH_3COO)_3$, 0.1 mmol $Yb(CH_3COO)_3$ and 0.1 mmol $Nd(CH_3COO)_3$ were mixed in a solution containing 10 mL OA and 15 mL ODE. The mixture was heated to 180 °C for 1 h to obtain a homogeneous solution. After the solution was cooled down to room temperature, the previously synthesized core-shell $NaYF_4$:Yb,Er@ $NaYF_4$:Yb NPs in 7.5 mL n-hexane were added along with 5 ml methanol containing 0.05 g NH_4F and 0.075 g NaOH. The mixture was heated to 100 °C to evaporate n-hexane and methanol before heating to 300 °C for 1.5 h. The mixture was cooled down to room temperature and the resulting core-shell-shell $NaYF_4$: Yb^{3+}(20%),Er^{3+}(2%)@$NaYF_4$:Yb^{3+}(20%)@$NaYF_4$:Yb^{3+}(20%),Nd^{3+}(20%) UCNPs were precipitated, washed with ethanol, collected by centrifugation and redispersed in 15 mL n-hexane. Yield 84 %. Elemental analysis data (ICP, ppm): Y, 8.48; Yb, 4.87; Er, 0.13; Nd, 1.17.

Coating of UCNPs with mesoporous silica ($mSiO_2$)

Coating $mSiO_2$ on the surface of oleate-capped UCNP was prepared according to the previously reported method[60]. Cetyltrimethyl-ammonium chloride (CTAC, 0.2 g) and the previously prepared core-shell-shell UCNPs (5 mg) were dissolved in 25 mL water at 50 °C with stirring overnight. The solution was sonicated for 30 min and 0.1 mL tetraethyl orthosilicate (TEOS), 150 µL 2 M NaOH and 1.5 mL ethyl acetate were added, and the resulting mixture was stirred for 2.5 h at 70 °C. After cooling down to room temperature, the rude product was collected by centrifugation and washed twice with 10 mL ethanol to remove the residual reactants. To remove the remaining CTAC, the rude product was further extracted with NH_4NO_3 (0.3 g) in 25 mL ethanol at 60 °C for 2 h, and cooled to room temperature. The $NaYF_4$:Yb,Er@$NaYF_4$:Yb@ $NaYF_4$:Yb, Nd@$mSiO_2$ or UCNP@$mSiO_2$ product was then obtained by centrifugation and washed with water.

Preparation of the IR806 PTS and loading/quantitation of IR806 dye in UCNP@ $mSiO_2$

The IR806 dye (2-((*E*)-2-((*E*)-2-((4-carboxy-phenyl)thio)-3-((*E*)-2-(3,3-dimethyl-1-propylindolin-2-ylidene)cyclohex-1-en-1-yl)vinyl)-3,3-dimethyl-1-propyl-3*H*-indol-1-ium iodide or simply IR806) was prepared according to the literature reported method using the IR780 iodide dye as the starting material (yield 53.6%)[56]. It was purified by HPLC, and characterized by NMR (e.g. ^{13}C NMR (101 MHz, $CDCl_3$): δ 172.49, 170.63, 148.89, 145.53, 144.47, 142.18, 141.04, 133.94, 131.07, 128.72, 126.70, 125.45, 125.31, 122.18, 111.00, 101.89, 49.20, 46.38, 27.84, 26.77, 20.93, 20.71, 11.68) and mass spectrometry (ESI-MS, $[M]^+$ calc. for $C_{43}H_{49}N_2O_2S^+$, 657.35(100.0%), 658.35(48.0%), 659.36(11.3%); found 657.4, 658.4, and 659.4). (Figure S1-S3, Supplementary materials). The molar extinction coefficient of IR806 in ddH_2O was determined to be 1.56 ± 0.08 x10^5 M^{-1}·cm^{-1} at 790 nm. Loading of IR806 to the UCNP@$mSiO_2$ was performed by mixing 5 mg UCNP@$mSiO_2$ with the respective

amounts of IR806 (i.e. 0.7 mg, 2.0 mg, and 2.5 mg) in 1 mL ethanol with sonication for 1 h. The UCNP@mSiO$_2$/IR806 was collected by centrifugation and washed with cold ethanol and redispersed in ddH$_2$O. Quantitation of the loaded IR806 was performed by spectrophotometry to be 4%, 15%, and 20% (wt%), respectively, using a literature published method with monor modification[61].

Preparations of UCNP@mSiO$_2$/IR806@PAH and UCNP@mSiO$_2$/IR806@PAH-PEG-FA

To obtain amino-functionalized nanocomposites, 5 mg UCNP@mSiO$_2$/IR806 was added to a 25 mL ethanol solution containing 50 µL PAH (20 wt%) and the mixture was stirred for 24 h at room temperature. The negatively charged UCNP@mSiO2/IR806 was coverd with the positively charged PAH by electrostatic interaction. The amino-functionalized nanocomposites UCNP@mSiO$_2$/IR806@ PAH were collected by centrifugation, washed with cold ethanol to remove unwanted components and the nanocomposites were re-dispersed in 10 mL water. The UCNP@mSiO$_2$/IR806@PAH in 10 mL water was further conjugated with 5 mg FA-PEG-NHS by amide bond formation. The mixture was stirred for 12 h at room temperature to obtain the final product UCNP@mSiO$_2$/IR806@PAH-PEG-FA (or UCNC-FAs), followed by centrifugation, washing and re-dispersion in water for further use. Quantitation of the loaded IR806 was performed by spectrophotometry to be 4%, 15%, and 20% (wt%), respectively, using a literature published method[60].

Stability and photothermal test

The stability of IR806 in nanocomposites was tested by dispersing 1 mg UCNC-FAs in 10 mL PBS buffer (pH 7.4), incubation for 24 h at room temperature, centrifugation, and the supernatant was quantified for the released IR806 by spectrophotometry. The photothemal test was performed by 793 nm NIR laser (2W/cm^2) irradiation at 3 mL solutions in cuvettes containing 1.5 mg/mL UCNC-FAs with different IR806 loading amounts (i.e. 0, 4, 15 and 20 wt%) for up to 30 h using a home-made set-up. The temperatures of the solutions were recorded at different time intervals by an electronic thermometer (Lutron Electronic enterprise). The photothermal conversion efficiency (η) was calculated by using the method reported by Roper[62, 63].

Cytotoxicity assays

The cytotoxity of the core-shell-shell UCNC-FAs containing 20 wt% IR806 was evaluated employing MDA-MB-231 cancer cells. The cells were seeded in 96-well plates (1 × 10^4 cells/well). After incubation in Dulbecco's Modified Eagle Medium (DMEM) for 24 h at 37 °C under 5% CO_2, 100 µL solutions of the UCNC-FAs in the concentration range of 3.9 - 1000 µg/mL were added into each well and incubated for 24 h and washed by PBS buffer. Then, 50 µl CCK-8 reagent (10 times dilution with DMEM) was added into each well. After incubation for 1.5 h at 37 °C, the cell viability was determined by measuring the absorbance at 450 nm in each well. The cytotoxicities of the free type IR806 and the UCNP@mSiO$_2$ NPs were measured in a similar way as that for UCNC-FAs. The data were shown as mean ± SD (n = 3).

In vitro cellular imaging

MDA-MB-231 cancer cells were seeded in six-well culture dishes at a concentration of 5 × 10^5 cells/well (2 mL) and incubated in DMEM for 24 hours at 37 °C under 5% CO_2 with and without the addition of the core-shell-shell UCNC-FAs (300 µg). All the cells were then incubated for 4 h and washed with PBS buffer solution to fully remove any excess UCNC-FAs. The cells were fixed by adding para-formaldehyde (2 wt%, 1 mL) in each culture dish for 10 min and the cell nuclei were stained with hoechst 33342 for 10 min. After washing with PBS solution, the cells were imaged using a laser confocal microscope (Olympus FV1000 & ZEISS LSM 880).

In vitro NIR induced PTT

MDA-MB-231 cancer cells were seeded in 96-well plates (1 × 10^4 cells/well) and incubated in DMEM for 24 h at 37 °C under 5% CO_2. Then 150 µL of the core-shell-shell UCNC-FAs (50 µg/mL, 20 wt% IR806) were added into each well and incubated for another 24 h. The treated cells (with UCNC-FAs) and the control group cells (without UCNC-FAs) were irradiated with a 793 nm laser (2W/cm^2) for 30 min, followed by incubation for another 24 h and addition of the CCK-8 reagent (50 µl, 10 times dilution with DMEM) to each well. After incubation for 1.5 h at 37 °C, the cell viability was determined by measuring the absorbance at 450 nm in each well. The data were shown as mean ± SD (n = 3).

Results and Discussion

Design, synthesis and characterizations of Nd^{3+} ion sensitized UCNPs

The absorption cross-section of the Nd^{3+} ion at 808 nm (i.e. 1.2 × 10^{-19} cm^2) was one order of magnitude greater than that of the Yb^{3+} ion at 980 nm (i.e. 1.2 × 10^{-20} cm^2)[64]. Because the peak of the Nd^{3+} ion at 793 nm is about 4 times higher than that at 808 nm in the down-conversion (to Yb^{3+} ion) excitation spectrum (λ_{em} = 980 nm, *vide infra*)[58], it is expected that even higher energy absorption efficiency would

result by excitation at 793 nm at the Nd^{3+} ion and provide deeper tissue penetration depth with less overheating than 980 nm irradiation at the Yb^{3+} ion. However, it was reported previously that the 793 nm irradiation at the Nd^{3+} ions in the $NaYF_4$ nanoparticles co-doped with the Yb^{3+} and Er^{3+} ions resulted in weak up-conversion luminescence by the Er^{3+} ions, even at the optimized Nd^{3+} and Er^{3+} ion concentrations (typically $\leq$ 1%), which was probably due in part to the re-absorption of the emission by the Nd^{3+} ions (i.e. from Er^{3+} to Nd^{3+} ^4I_J manifolds)[54, 57]. It was further reported that without the synchronous doping of the Nd^{3+} and Yb^{3+} ions in the lattice, the emission intensities of several Er^{3+} ion-doped $NaYF_4$ nanomaterials were too weak to be observed clearly[65]. Thus, the core-shell-shell nanoparticles comprising the lanthanide Nd^{3+}, Yb^{3+} and Er^{3+} ions in the $NaYF_4$ lattice were proposed to be used by us for the up-conversion luminescence imaging with 793 nm irradiation. The Er^{3+} ions act as the receptors and the Nd^{3+} and Yb^{3+} ions serve as the donors and mediators, respectively. By design, the Er^{3+} and Nd^{3+}/Yb^{3+} ions are separately doped in the core and the outer shell layer, respectively, and divided by a middle Yb^{3+} ion shell[58], to increase the up-conversion efficiency and to reduce the energy back transfer from the Er^{3+} ions to the Nd^{3+} ions. The middle shell also increases the distance between the core Er^{3+} emitters and the outer surface to reduce surface quenching and non-radiative relaxation. Note that the mole% of Er^{3+} ion in the core and Nd^{3+} ion in the outer shell were purposely limited to 2% and 20%, respectively, to avoid luminescence concentration quenching.

Our UCNPs design was different from another reported nanomaterial $NaYF_4$:Yb(20%),Er(2%)@ $NaYF_4$:Yb(20%)@$NaNdF_4$:Yb(10%) UCNPs in which the outer shell was $NaNdF_4$:Yb(10%)[55], presumably to maximize the absoption of the NIR light by the Nd^{3+} ions, although optimization was still needed because high absorption may lead to luminescence concentration quenching. It turned out that our current outer shell composition of $NaYF_4$:Nd^{3+}(20%), Yb^{3+}(20%) was exactly that of the optimized for luminescence imaging reported very recently[66]. The synthetic approach of our NPs was also different from theirs, in that our NPs were made directly in the β-forms and their β-NPs were made through the α-form intermediates. Note that subtle differences in preparations may lead to nanoparticles with different morphologies and perhaps different photophysical properties (*vide infra*)[67]. Figure 1 shows the TEM images and DLS analysis results of the core $NaYF_4$:Yb,Er NPs, the core-shell $NaYF_4$:Yb,Er@ $NaYF_4$:Yb NPs and the core-shell-shell $NaYF_4$:Yb,Er@ $NaYF_4$:Yb@ $NaYF_4$:Yb,Nd UCNPs, as well as their X-ray diffraction pattens.

From the TEM images it is observed that the NPs and UCNPs are uniform in size with regular hexagonal shapes and the average sizes are in the order core < core-shell < core-shell-shell (Figure 1, A-C). XRD pattens of the core, core-shell and core-shell-shell NPs confirm that these nanomaterials are in hexagonal phases by comparing with JCPDS No.16-0334 β-NaYF4 (Figure 1, G). Assuming the NPs and UCNPs are all cylindrical, the respective hexagonal diameters (D) and heights (H) were estimated to be D_{core} = 17.6 nm, H_{core} = 23.5 nm; $D_{core\text{-}shell1}$ = 20.6 nm, $H_{core\text{-}shell1}$ = 32.3 nm; $D_{core\text{-}shell1\text{-}shell2}$ = 25 nm, $H_{core\text{-}shell1\text{-}shell2}$ = 41 nm for the core/core-shell NPs and core-shell-shell UCNPs, respectively (SD ~ 0.5 – 1.2 nm). These are smaller than but in accord with that estimated by the DLS measurements of the monodispersive nanoparticles with very low polydispersity index (PdI) values of 0.121, 0.117 and 0.108, respectively (Figure 1, D-F)[68]. The average thickness estimated by the DLS data was 5 nm for the first shell and 2.5 nm for the second shell. The particle sizes by DLS analyses are larger than those of TEM measurements which has been reported previously[69-71].

On the other hand, an interesting anisotropic shell growth of the NPs was noted by comparing the unequal shell thickness of each shell estimated from TEM images, i.e. from the values of hexagonal diameters and heights, the values of the shell thickness of ΔD_{shelli} and ΔH_{shelli} (i = 1 or 2) were calculated to be: $\Delta D_{shell1} = (D_{core\text{-}shell1} - D_{core})/2$ = 1.5 nm, $\Delta H_{shell1} = (H_{core\text{-}shell1} - H_{core})/2$ = 4.4 nm; $\Delta D_{shell2} = (D_{core\text{-}shell1\text{-}shell2} - D_{core\text{-}shell1})/2$ = 2.2 nm, $\Delta H_{shell2} = (H_{core\text{-}shell1\text{-}shell2} - H_{core\text{-}shell1})/2$ = 4.35 nm. The H/D aspect ratios for the core, core-shell and core-shell-shell NPs were 1.34, 1.57 and 1.64, respectively. The $\Delta H_{shell1}/\Delta D_{shell1}$ and $\Delta H_{shell2}/\Delta D_{shell2}$ values were 2.9 and 2.0, respectively. In a previous paper it was stated that the prevalence of anisotropic shell growth in many up-conversion $NaLnF_4$ systems was caused by a combination of factors: selective adsorption of ligands on the core surface due to the core crystal structure, ligand etching, and the lattice mismatch between core and shell components[72]. It was claimed that the shell growth was highly anisotropic in the oleic acid synthesis system: the shell tended to grow from the six lateral faces rather than along the perpendicular axis to the hexagonal face, especially when the shell was thin. For example, in the cases of core-shell $NaYF_4$:Yb^{3+}(20%),Er^{3+}(2%)@$NaYbF_4$ and $NaYF_4$:Yb^{3+}(20%),Er^{3+}(2%)@$NaGdF_4$, unlike the $NaYbF_4$ shell, the $NaGdF_4$ shell only grew on the side faces regardless of the shell thickness, due to relatively large lattice mismatch between the $NaGdF_4$

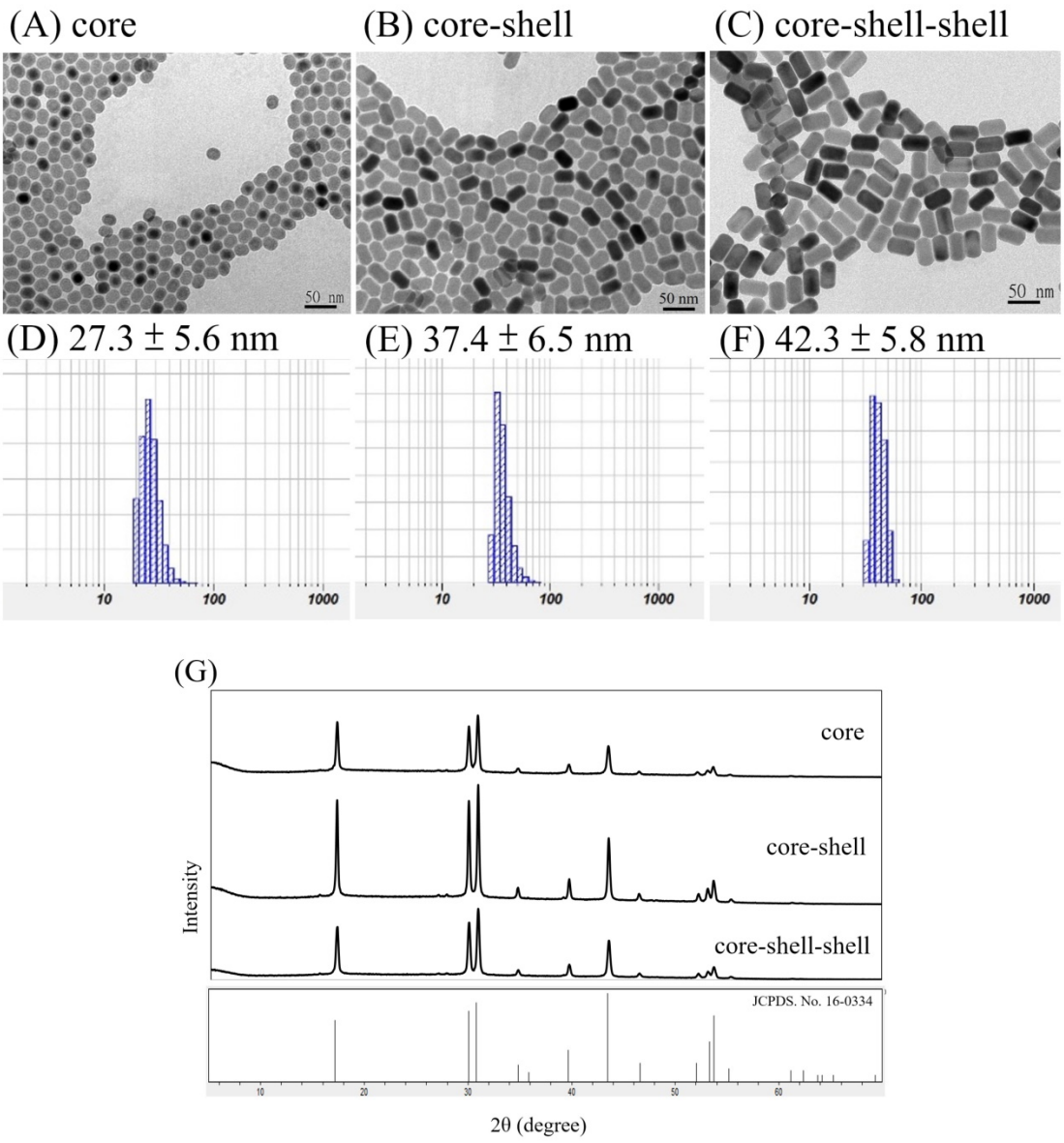

Figure 1. TEM images (A-C) and DLS results (D-F, in water) of core $NaYF_4$:Yb,Er NPs (A, D), core-shell $NaYF_4$:Yb,Er@$NaYF_4$:Yb NPs (B, E) and core-shell-shell $NaYF_4$:Yb,Er@$NaYF_4$:Yb@ $NaYF_4$:Yb,Nd UCNPs (C, F); scale bar = 50 nm. XRD pattens (G) of the core NPs, core-shell NPs and core-shell-shell UCNPs are in hexagonal phases by comparing with JCPDS No.16-0334 β-NaYF4.

shell and the $NaYF_4$ core, as well as the different ionic radii of Y^{3+} and Gd^{3+} ions. The Nd^{3+} ion in our UCNPs are larger than the Gd^{3+} ion, however, the shell growth was more along the perpendicular axis. Thus, it was more likely that by the control over the ratio of oleate anions (OA^-) to oleic acid molecules (OAH), the crystallographic facets of the nanoparticles could be directionally inhibited, promoted or etched, which enabled selective grafting of shells with complex morphologies grown over nanocrystal cores[67].

From the TEM images we were able to estimate the volumes of the core and shells in these NPs according to a literature publised method with minor modifications[73] (Method S1, Supplementary materials). At the added 1:1:2 mole ratio for the core:first shell:second shell starting material mixtures, the core:first shell:second shell volume ratio was found to be about 1:0.88:1.64 after the reaction and purification, indicating that the loading efficiency was gradually reduced as the number of shells was increased from one to two. A unique method to compare the wt% and mole% compositions calculated by using the morphological images and the inductively coupled plasma (ICP) elemental analysis data of the core, core-shell and core-shell-shell NPs can now be developed. Assuming these NPs are cylindrical and the volume ratios are similar to mole ratios, the theoretical (based on starting reaction mole% data), calculated (based on TEM images) and experimentally determined (based on ICP data) wt% and mole% compositions of Y^{3+}, Yb^{3+}, Er^{3+} and Nd^{3+} in the core, core-shell and core-shell-shell NPs were

calculated and listed in Table 1. Detailed examples of calculations are also shown in Method S1 (Supplementary materials). In general, the calculated results based on the TEM images and ICP data were quite consistent, as compared with those of the theoretcally expected. It is interesting to note that the differences between TEM estimated and the ICP data determined wt% and mole% for Y^{3+}, Yb^{3+}, Er^{3+} and Nd^{3+} are -1.2%, +1.7%, -0.2% and -0.3%, respectively. These discrepancies might result from the difficulties of handling small quantities of the hygroscopic starting materials as well as the errors due to ICP determinations[74].

Table 1. The theoretical (based on starting reaction mole% data), calculated (based on TEM images) and experimentally determined (based on ICP data) wt% and mole% compositions of Y^{3+}, Yb^{3+}, Er^{3+} and Nd^{3+} in the core, core-shell and core-shell-shell NPs.

NPs		core		core-shell		core-shell-shell	
Compositions		wt %	mol %	wt %	mol %	wt %	mol %
Theoretical calculation	Y	64.6%	78.0%	65.9%	79.0%	58.8%	72.7%
	Yb	32.3%	20.0%	32.5%	20.0%	31.5%	20.0%
	Er	3.1%	2.0%	1.6%	1.0%	1.0%	0.7%
	Nd					8.7%	6.7%
Calculated from TEM images	Y	64.6%	78.0%	65.9%	78.9%	59.1%	72.9%
	Yb	32.3%	20.0%	32.5%	20.0%	31.5%	20.0%
	Er	3.1%	2.0%	1.7%	1.1%	1.1%	0.7%
	Nd					8.3%	6.3%
Determined from ICP data	Y	63.9%	77.4%	63.4%	77.1%	57.9%	72.0%
	Yb	32.7%	20.3%	34.9%	21.8%	33.2%	21.3%
	Er	3.5%	2.2%	1.7%	1.1%	0.9%	0.6%
	Nd					8.0%	6.1%

The EDS data for the core-shell-shell sample was obtained to directly observe the distribution of the Y^{3+}, Nd^{3+} and Yb^{3+} ions (Figure S4, Supplementary materials). The Er^{3+} ions were confined in the inner region, thus could not be detected at outer region, similar to that reported previously[55]. The high-resolution transmission electron microscopy (HRTEM) images of the core-shell-shell UCNPs and UCNP@$mSiO_2$ were also attached. (Figure S5, Supplementary materials). Because the base material is $NaYF_4$, the layers in the core-shell-shell structure could not be observed, which was also similar to that reported previously[58]. However, the increasing sizes and the ICP data analysis clearly showed the core, core-shell and core-shell-shell formations and the presence of each Ln^{III} ion in the UCNPs.

Photophysical properties of NPs

The luminescence spectra of the NPs in n-hexane with 125 mW/cm^2 continuous wave NIR radiations at 980 nm or 793 nm are shown in Figure 2.

It is observed in Figures 2A that the Yb^{3+} to Er^{3+} up-conversion emission peak intensities at 520 nm ($^2H_{11/2} \rightarrow {}^4I_{15/2}$), 540 nm ($^4S_{3/2} \rightarrow {}^4I_{15/2}$) and 654 nm ($^4F_{9/2} \rightarrow {}^4I_{15/2}$) increase with incresing number of shells added from the core $NaYF_4$:Yb,Er NPs to the core-shell $NaYF_4$:Yb,Er@$NaYF_4$:Yb NPs, and to the core-shell-shell $NaYF_4$:Yb,Er@$NaYF_4$:Yb @$NaYF_4$:Yb, Nd UCNPs at λ_{ex} = 980 nm in n-hexane. This confirms the effects of the shells in facilitating the energy transfer, probably by decreasing surface crystal defect and quenching. At similar concentrations, the emission intensities at 520, 540 and 654 nm of the core-shell-shell UCNPs increased about 8, 7.9 and 3 times than those of the core NPs, respectively. On the other hand, excitation at 793 nm could also produce up-conversion energy transfer from the Nd^{3+} ions in the core-shell-shell $NaYF_4$:Yb,Er@$NaYF_4$:Yb@$NaYF_4$:Yb,Nd UCNPs to the Er^{3+} ions *via* $Nd^{3+} \rightarrow Yb^{3+} \rightarrow Er^{3+}$ (*vide infra*) to result in the peak maxima at 520 nm, 540 nm and 654 nm which were consistent with that reported in the literature (Figure 2B)[54].

The down-conversion energy transfer from the Nd^{3+} ions in the core-shell-shell UCNPs excited at 793 nm to the Yb^{3+} ions could be confirmed by the emission spectrum in the NIR region (Figure 2C, λ_{max} = 980 nm, due to the $^2F_{5/2} \rightarrow {}^2F_{7/2}$ transition). Figure 2C (inset) also shows the excitation spectrum of the core-shell-shell UCNPs in the 720-810 nm wavelength region (λ_{em} = 980 nm), and analysis of the spectrum indicating excitation at 793 nm is about 4 times stronger than that at 808 nm for the down-conversion to 980 nm (*vide supra*). NIR lights have low scattering characteristics which are more suitable for deep-tissue luminescence imaging than the visible lights, and would be at least useful in small animal models for pharmacokinetic studies and monitoring drug effectiveness.

Surface modification of UCNPs

The surface of the core-shell-shell UCNPs is relatively hydrophobic and is preferably modified with hydrophilic materials for biomedical applications. In this regard, we have used the mesoporous silica ($mSiO_2$) to modify our UCNPs for larger surface area and more pores to load photosensitizers for PDT[61, 75, 76] or chemo-drugs[77], *via* physisorption or covalent bond formation, which could be delivered to the tumor sites through the well-known enhanced permeability and retention (EPR) effect[78]. This was done by using CTAC as the surfactant and porous template to help polymerization of $mSiO_2$ to cover the UCNPs surface. The resulted UCNP@$mSiO_2$ product could be evenly dispersed in aqueous solution and TEM image confirmed that the $mSiO_2$ shell was coated on the surface (Figure 3A). The average diameter of the nanoparticles was about 73 nm and the thickness of the $mSiO_2$ layer was about 20 nm with clearly visible

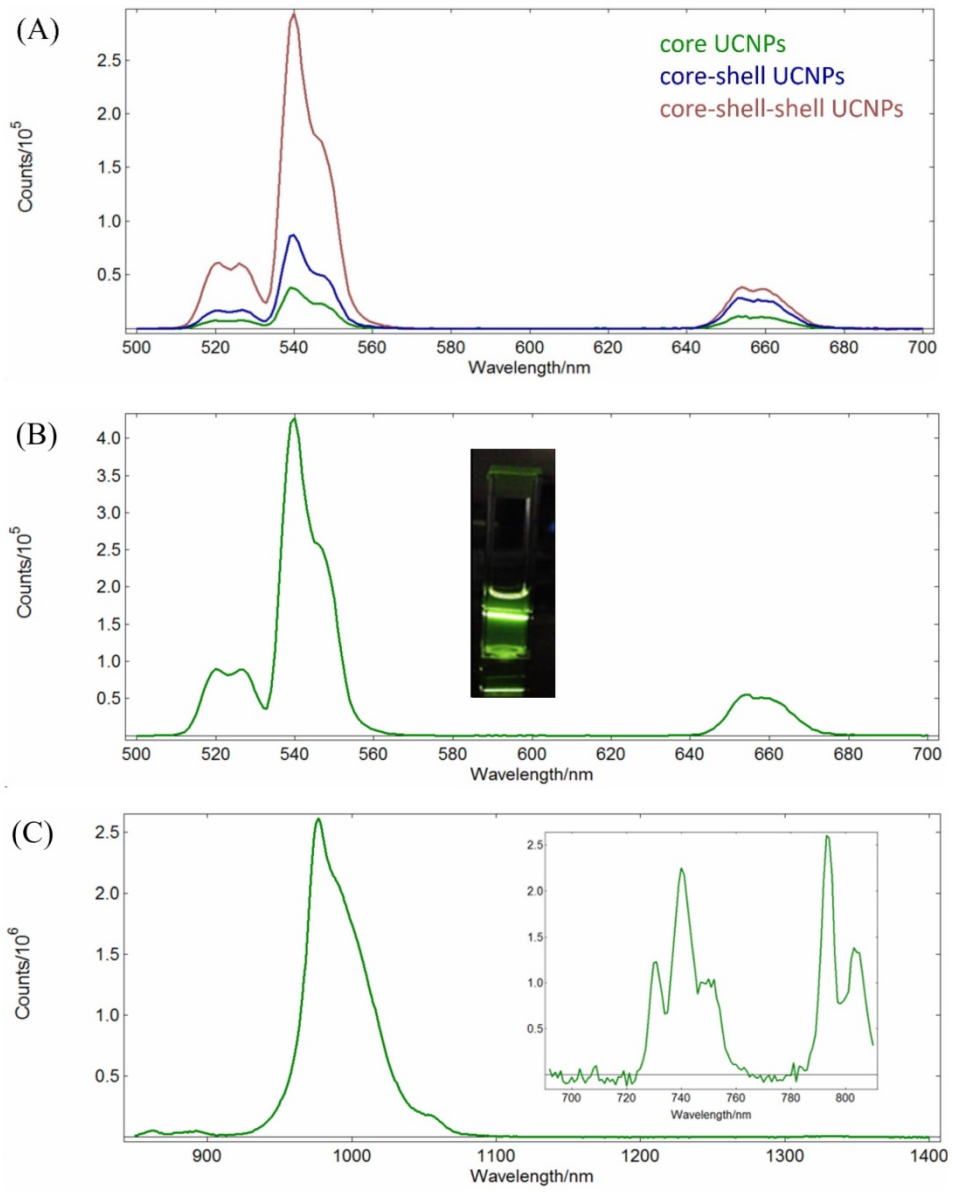

Figure 2. (A) Up-conversion emission spectra of the core $NaYF_4$:Yb,Er NPs (green), the core-shell $NaYF_4$:Yb,Er@$NaYF_4$:Yb NPs (blue), and the core-shell-shell $NaYF_4$:Yb,Er@$NaYF_4$:Yb@$NaYF_4$: Yb,Nd UCNPs (red); λ_{ex} = 980 nm, 1 mg/mL in n-hexane. (B) Up-conversion emission spectrum of $NaYF_4$:Yb, Er@$NaYF_4$:Yb@$NaYF_4$:Yb,Nd core-shell-shell UCNPs (λ_{ex} = 793 nm, 1 mg/mL in n-hexane; inset: photograph of the sample solution). (C) Down-conversion emission spectrum (λ_{ex} = 793 nm, 1 mg/mL in n-hexane) and excitation spectrum (λ_{em}= 980 nm, inset) of $NaYF_4$:Yb,Er@ $NaYF_4$:Yb@ $NaYF_4$:Yb,Nd UCNPs.

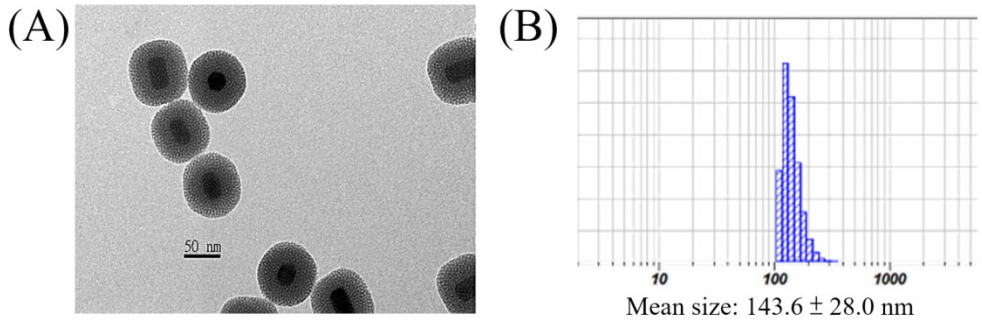

Figure 3. (A) TEM image and (B) DLS result of the UCNP@$mSiO_2$.

pores. DLS analysis gave a larger average diameter of 143.6 ± 28.0 nm (Figure 3B).

The zeta potential of the freshly prepared UCNP@$mSiO_2$ containing some residual CTAC was +30.5 mv. After washing with NaCl methanol solution to remove the residual CTAC, the zeta potential was -10.9 mV. Further loading of the photosensitizer IR806 (20 wt%) in the pores and coating with positively

charged PAH containing NH_2 functional groups to prevent the loss of IR806[79], the zeta potential of the resulted UCNP@mSiO$_2$/IR806@PAH was +81.2 mV. If the FA-PEG-NHS ester was covalently bonded to the nanoparticles *via* peptide bond formation with the NH_2 functional groups for active tumor targeting[80], the zeta potential of the final UCNP@mSiO$_2$/IR806 @PAH/PEG-FA nanocomposite was +65.3 mv. Using this nanocomposite at concentrations from 3.9 to 62.5 μg/mL, the dark cell viabilities were all greater than 85%, indicating that this material was rather safe for further biological and preclinical tests (*vide infra*). Note that an optimized zeta potential of this type of nanocomposites for future practical biological and clinical applications is currently unknown, however, it could be easily reduced by adding the loaded amount of PEG-FA if needed[81]. Detailed TEM images, DLS analysis and Zeta-potential measurements of UCNP@mSiO$_2$/ IR806@PAH and UCNP@mSiO$_2$/IR806@PAH/PEG-FA are shown in Figure S6 (Supplementary materials).

The absorption peak maximum of IR806 is at 790 nm. The UCNPs after loading IR806 became dark green and the peak maximum was red-shifted to 800 nm (Figure S7, Supplementary materials)[82]. On the other hand, the up-conversion emission spectra of the UCNPs in n-hexane as well as the UCNP@mSiO$_2$ and UCNP@mSiO$_2$/IR806(20 wt%)@PAH/PEG-FA (or UCNC-FAs) in aqueous solutions are shown in Figure 4.

Unlike our previous study of the Gd_2O_2S:Eu nanoparticles which lost most of luminescence in moving from n-hexane to aqueous solution[83], our currently prepared UCNPs and UCNP@mSiO$_2$ retained about 80% emission intensities at 540 nm. However, after loading IR806 (20 wt%), the emission intensity at 540 nm was reduced to about 1/7 of that of UCNP@mSiO$_2$, probably because IR806 absorbed most of the light at 793 nm due to much higher molar absorptivity than the Nd^{3+} ion, although it was possible for the IR806 to transfer energy to Nd^{3+}[84, 85]. As mentioned previously, lower IR806 loading would increase the emission intensity at the expense of decreasing its photothermal efficacy (*vide infra*)[86]. Note that the Er^{3+} ions in the UCNPs core were well shielded by the shells and their optical properties, i.e. lifetimes and emission intensities should not be affected by the outer surface modifications[87]. The absorption spectrum of IR806 in the present nanocomposites had little overlap with the emission spectrum of the Er^{3+} ion. Thus, as the up-conversion receptor, the Er^{3+} ion would be expected to function as an effective imaging mediator.

The 650-670 nm band emission intensity after loading IR806 (20 wt%) was about 50% of that without loading. This is typical for the up-conversion nanomaterials for which the emission band intensities at different wavelengths will change with excitation power density, as well as composition, structure, size and shape[88-90]. For example, the respective $NaYF_4$:Yb^{3+},Er^{3+} red (650 nm)-to-green(540 nm) emission intensity ratios excited at 45 and 150 W/cm^2 are 1.05 and 1.45, which is not proportional to their excitation power. In the absence of a suitable equipment to measure the up-conversion quantum yield, we cited an unoptimized up-conversion absolute quantum yield of a similar quenching-shield sandwich structure $NaYF_4$:Yb,Er@$NaYF_4$:Yb@NaNd F_4:Yb UCNPs at 540 nm to be 0.11 ± 0.05% under excitation at 800 nm (20W/cm^2)[55]. Although it is possible to further optimize the IR806 loading amount and the lanthanide doping percentages to achieve better emission imaging as well as photothermal effect[84, 86], such subtle adjustments would be quite complicated and were not appropriate at the current proof-of-principle stage.

The amount of loaded IR806 onto the core-shell-shell UCNC-FAs was estimated by subtracting the unreacted IR806 in the reaction supernatant after centrifugation from the total added

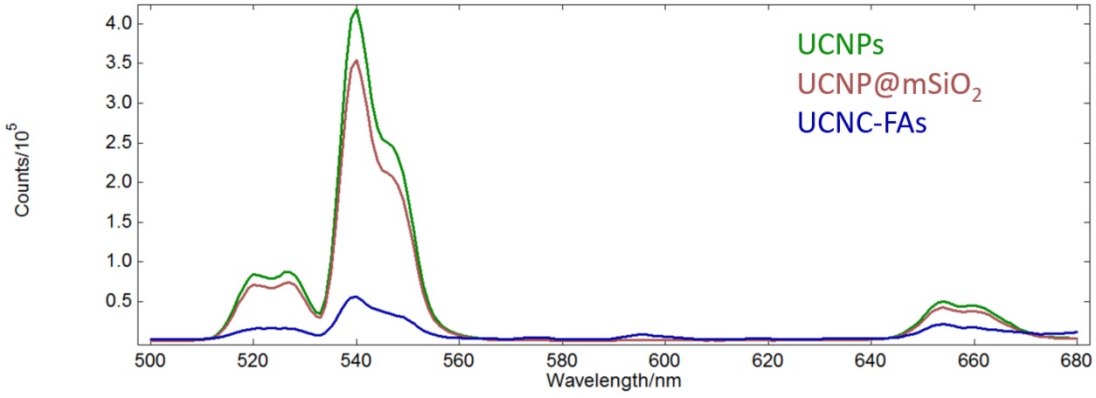

Figure 4. Up-conversion emission spectra of the UCNPs in n-hexane (green) as well as UCNP@mSiO$_2$ (purple) and UCNP@mSiO$_2$/IR806(20 wt%)@PAH/PEG-FA (blue) in aqueous solutions (λ_{ex} = 793 nm, 1 mg/mL).

IR806 using equation 1. A standard IR806 calibration curve was prepared to determine the unreacted IR806 and the loaded amount of IR806 was about 20 wt% when 2.5 mg IR806 was added to 5 mg UCNPs. Other loaded amounts of IR806 on the UCNC-FAs could be obtained by varying the relative amounts of IR806 and UCNPs. The stability test of the loaded IR806 in 1 mg nanocomposites in 10 mL PBS bufter (pH 7.4) after 24 h showed less than 5% of the IR806 was released to the supernatant indicating more than 95% IR806 was still in the UCNC-FAs.

$$\text{IR806 loading}(\%) = \frac{\text{Mass of IR806 incorporated into paticles}}{\text{Mass of particles}} \times 100\% \quad (1)$$

Photothermal test

The photothermal test was performed using UCNC-FAs aqueous solutions containing varying amounts of loaded IR806 with pure water as the control. Figure 5A shows that the solution temperature was increased with increasing 793 nm radiation time at 2W/cm² starting at 29.3 °C. After 20 min irradiation, the respective temperatures were 38.9 °C, 40.5 °C, 42.3 °C and 45.4 °C for the UCNC-FAs solutions containing 0%, 4%, 15% and 20% IR806. The respective temperatures increased were 9.6 °C, 11.2 °C, 13.0 °C and 16.1 °C which varied linearly with increasing amount of loaded IR806 (Figure 5B).

The respective slope and intercept of the linear regression analysis at 10 min heating time were 0.25 °C/$\%_{IR806}$ and 8.25°C (r^2 = 0.97); and at 20 min heating time, 0.30 °C/$\%_{IR806}$ and 9.61°C (r^2 = 0.92). Specifically, for the UCNC-FAs with 20% loaded IR806, the temperature was raised to 42.4 °C with 10 min irradiation. This confirms that the UCNC-FAs could be used for further biological studies for photothermal therapy. Note that the 808 nm radiation at 1~2W/cm²[15], 3.8W/cm² [19] and 6W/cm² [18] were all reported which did not cause cell damage in the absence of the PTT agents. These results were similar to ours with 793 nm radiation at 2W/cm².

The photothermal conversion efficiency (η) of the UCNC-FAs with 20% loaded IR806 was calculated to be 46% by the method published previously [62, 63] (Method S2, supplementary materials), which was higher than that (i.e. 17-21%) using ICG and commercially available gold nanorods, respectively[63, 91], but lower than that (i.e. 88%) of graphene-IR780[92]. Note that the radius of irradiating area of our 793 nm NIR laser equipped with a collimator was about 15 mm, which was greater than those (i.e. ≤ 3 mm) of other studies, e.g. using 808 nm laser without collimator. A larger and controllable NIR irradiation area could be potentially beneficial for *in vivo* photothermal therapy against cancer due to its flexibility to adjust the irradiation area based on the sizes of the diseased tissue needed.

Cell viability test

The use of the $mSiO_2$ layer to load IR806 in the pores and further coating with PAH/PEG-FA was designed to increase the IR806 loading with high dark cell viability without light radiation, and to exert high cell toxicity with photo-excitation. The UCNC-FAs containing 20% IR806 in different concentrations were mixed with the MDA-MB-231 cancer cells in dark for 24 h and the measured cell viabilities were compared with those of free type IR806 in the 0 - 32 μg/mL concentration range (Figure 6A). It was observed that free type IR806 was much more toxic than that loaded in the UCNC-FAs. For example, free type IR806 at 4 μg/mL exerted a cell viability of 23% (i.e. IC_{50} ~ 1.7 μg/mL) which was much lower than the cell viability when 12.5 μg/mL of IR806 was loaded in the UCNPs, i.e. 85% (i.e. IC_{50} > 100 μg/mL). This was in contrast to the IR780 iodide for which the dark viabilities were

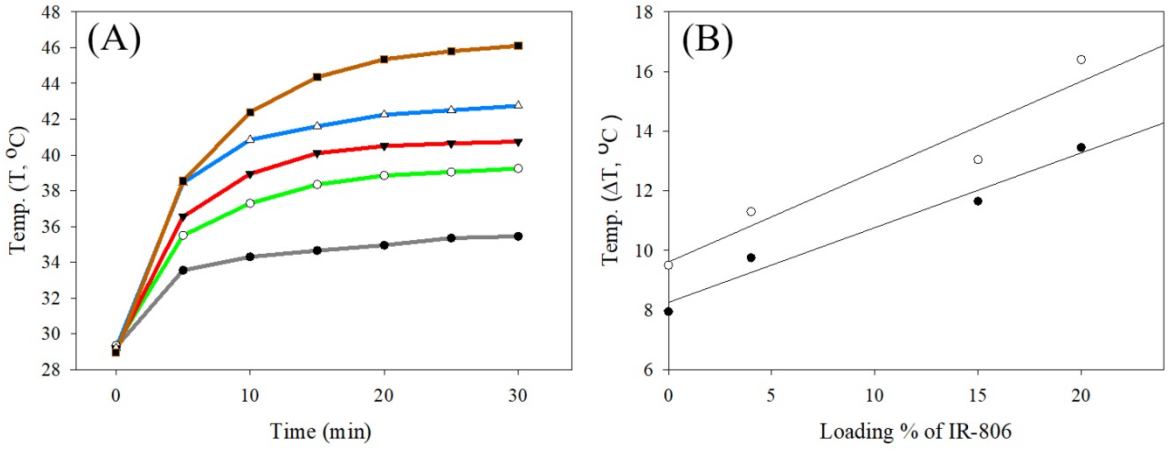

Figure 5. (A) Plots of temperature vs. 793 nm radiation time (2W/cm²) starting at 29.3 for various UCNC-FAs aqueous solutions containing varying wt% of loaded IR806: black, pure water; green, 0%; red, 4%; blue, 15%; brown, 20%. [UCNC-FAs] = 1.5 mg/mL. (B) Linear regression analysis of temperature increased (ΔT, °C) vs. loading % of IR806 after 10 min (●) and 20 min (○) heating with 793 nm laser.

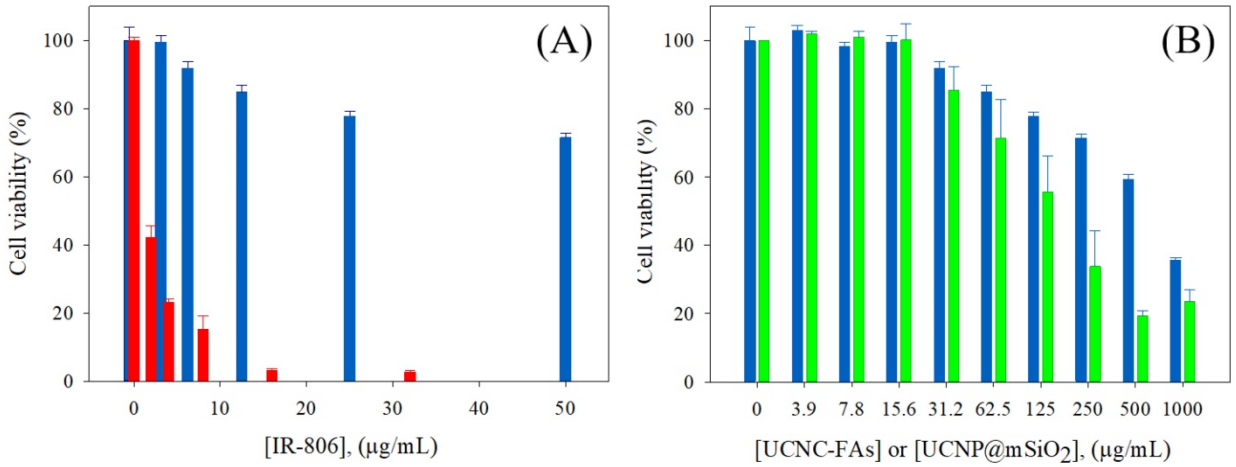

Figure 6. (A) Dark MDA-MB-231cell viability by incubation with different concentrations of IR806: free type (red); loaded in the UCNC-FAs (blue). (B) Dark MDA-MB-231cell viability by incubation with different concentrations of UCNC-FAs containing 20 wt% IR806 (blue) and UCNP@mSiO$_2$ (green).

not much different between the free type and formulated heparine-folic acid-IR-780 nanoparticles by self-assembly[5]. In addition, the dark MDA-MB-231 cell viabilities of the UCNP@mSiO$_2$ NPs without IR806 were all lower as compared to those of UCNC-FAs at concentrations greater than 62.5 μg/mL, i.e. $P < 0.05$ (Figure 6B). Note that the cell internalization of UCNC-FAs is likely higher than that of UCNP@mSiO$_2$ NPs without IR806 due most likely to the folate-mediated endocytosis (*vide infra*), its cell viabilities are greater as compared to those of UCNP@mSiO$_2$ NPs without IR806, presumably due to the protective PEG coating on the UCNC-FAs [61, 93].

In vitro Cell imaging

Figure 7 shows the confocal laser scanning microscope images of the MDA-MB-231 cells incubated with and without UCNC-FAs. Because the up-conversion luminescence imaging equipment is still under development, the cell images were obtained with 488 nm direct irradiation at the Er^{3+} ions. It was observed that the UCNC-FAs were clearly distributed in the cytoplasm of the cells, most likely through the well-known folate-mediated endocytosis as has been demonstrated in many cases[12, 39, 60] and possibly the electrostatic interactions between the particles and cell membranes. Note that if a 793 nm laser radiation source was used for similar *in vivo* imaging study, the result would be expected to be much better than that using the 488 nm radiation due to better penetration depth ability of the 793 nm laser.

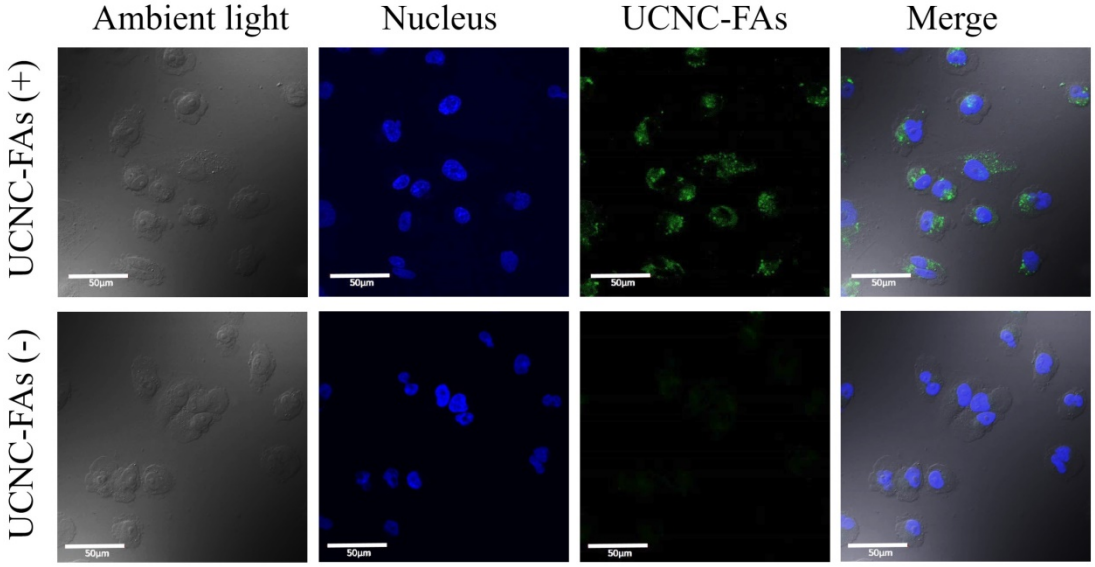

Figure 7. Confocal laser scanning microscope luminescence imaging of MDA-MB-231 cells incubated with and without UCNC-FAs. Cell nuclei stained with Hoechst 33342 were shown in blue. The luminescence signal of UCNC-FAs was displayed in green. No luminescence in the control group was observed when the cells were not treated with the UCNC-FAs.

In vitro photothermal therapy

Figure 8 shows that in the presence of 31.25 μg/mL and 62.5 μg/mL UCNC-FAs (containing 20 wt% IR806), the respective MDA-MB-231 cell viabilities after 793 nm irradiation at 2 W/cm² for 30 min decreaded to 71% from the control 97% (P = 0.0317) and to 49% from the control 86% (P = 0.0092), indicating that the UCNC-FAs prepared in the current study are quite effective as potential drugs for photothermal therapy. The cells without UCNC-FAs under similar NIR irradiation were not affected.

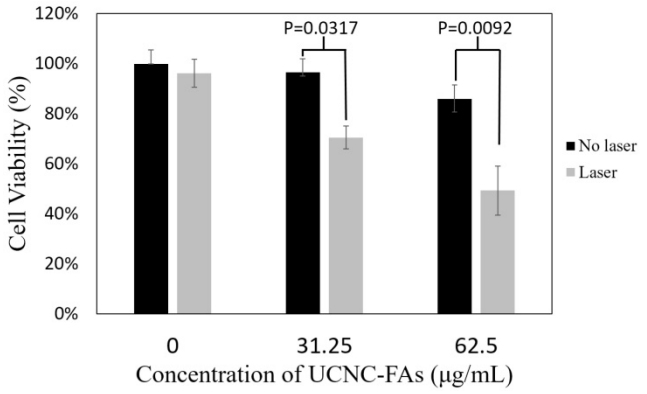

Figure 8. *In vitro* photothermal therapy efficiency using different concentrations (31.25 μg/mL and 62.5 μg/mL) of UCNC-FAs (containing 20 wt% IR806) under 2W/cm² 793 nm laser irradiation. Control group was incubated with the nanocomposite without light treatment.

The *in vivo* targeting, imaging and PTT efficacy studies will be performed at a later stage if the optimized nanocomposite becomes a potential drug candidate as compared to others under current study to warrant for further preclinical tests.

Conclusion

In conclusion, we have designed and prepared a novel nanocomposite (i.e. UCNP@mSiO$_2$/IR806@PAH-PEG-FA or UCNC-FAs) combining the PTS IR806 and Nd^{3+} sensitized core-shell-shell $NaYF_4$:Yb,Er@$NaYF_4$:Yb@$NaYF_4$:Yb,Nd UCNPs, and demonstrated that it is possible to use a single wavelength 793 nm light irradiation to perform photothermal therapy (PTT) and luminescence imaging using this theranostic nanomaterial. This approach is more convenient to use for deeper-tissue penetration and to reduce overheating problems when compared with irradiation at 980 nm. Both up- and down-conversion energy transfers to allow emissions in the visible and NIR wavelength regions are possible for luminescence imaging. Loading of IR806 in the mSiO$_2$ pores and protection by PAH-PEG-FA coating make the nanacomposites to be much more viable as compared to the free type IR806 dye. *In vitro* studies using the MDA-MB-231 cancer cells showed that the UCNC-FAs with folate (FA) functional groups could facilitate cell endocytosis, making it a potentially effective theranostic drug for targeted PTT and luminescence imaging when irradiated by a single NIR 793 nm laser.

Future work will extend this platform to optimize the photophysical properties and the loading effectiveness of the photothermal and/or imaging sensitizers, and to improve the biocompatibilities of the nanocomposites. Additional preclinical *in vivo* animal model studies including NIR up-conversion and down-conversion luminescence imaging with high signal-to-noise ratios, and hopefully clinical evaluations of potential theranostic drug candidates are also needed for effective targeted photothermal therapy and luminescence imaging using a single NIR light radiation, emplying core-shell like nanocomposites containing, e.g. $NaLnF_4$:Ln'@TiO_2 or other photosensitizers (Ln = Y, Gd; Ln' = Nd, Er, Tm, Yb).

Abbreviations

CT, computed tomography; CTAC, n-hexadecyl-trimethylammonim chloride; DMEM, Dulbecco's Modified Eagle Medium; EDS, Energy-dispersive X-ray spectroscopy; HRTEM, High Resolution Transmission Electron Microscopy; ICG, indocyanine green; ICP-OES, inductively coupled plasma optical emission spectrometry; Ln, lanthanide; MRI, magnetic resonance imaging; mSiO2, mesoporous silica; NIR, near infrared; OA, oleic acid; ODE, octadecene; PAI, photoacoustic imaging; PAH, polyallylamine; PDT, photodynamic therapy; PET, positron-emission tomography; PEG-FA, polyethylene glycol-folic acid; PS, photosensitizers; PTS, photothermal sensitizers; PTT, photothermal therapy; SPIO, superparamagnetic iron oxide nanoparticles; SWNTs, single-walled carbon nanotubes; TEM, transmission electron microscope; TEOS, tetraethyl orthosilicate; UCNC-Fas, UCNP@mSiO2/IR806@PAH-PEG-FA nanocomposites; UCNP, up-conversion nanoparticles; WBH, whole-body hyperthermia; XRD, X-ray powder diffraction.

Acknowledgments

This research was supported by the Ministry of Science and Technology of Taiwan (NSC102-2627-E-010-001, NSC102-2627-M-010-001, MOST103–2627-M-010–001, MOST104-2627-M-010-001, MOS T105-2113-M-010-001, MOST106-2113-M-010-006), Veterans General Hospitals University System of Taiwan Joint Research Program (VGHUST104-G7–4–1), Taiwan (ROC) and the Professor Tsuei-Chu Mong Merit Scholarship of National Yang-Ming University (to S-L Lin).

Supplementary Material

Geometric TEM morphological and ICP data analysis of core, core-shell and core-shell-shell UCNPs in Method S1; calculation of the photothermal conversion efficiencies (η) for FA-UCNCs in Method S2; ^{1}H-NMR, ^{13}C-NMR and 2D-NMR of IR806; mass spectra of IR806; HPLC chromatograms of IR806 and IR780; the EDS data of the core-shell-shell UCNPs; HR-TEM images of the core-shell-shell UCNPs; TEM images, DLS measurements and zeta potenital measurements of UCNPs@mSiO_2 /IR806@PAH and UCNPs@mSiO_2/IR806@PAH/PEG-FA; absorption spectra of free type IR806 and IR806 in UCNC-FAs (blue) in Figures S1-S7.
http://www.ntno.org/v02p0243s1.pdf

Competing Interests

The authors have declared that no competing interest exists.

References

1. DeVita Jr VT, Rosenberg SA. Two hundred years of cancer research. N Engl J Med. 2012; 366: 2207-14.
2. Rosenberg SA, Yang JC, Restifo NP. Cancer immunotherapy: moving beyond current vaccines. Nat Med. 2004; 10: 909.
3. Tsuruo T, Naito M, Tomida A, Fujita N, Mashima T, Sakamoto H, et al. Molecular targeting therapy of cancer: drug resistance, apoptosis and survival signal. Cancer Sci. 2003; 94: 15-21.
4. Wang D, Xue B, Kong X, Tu L, Liu X, Zhang Y, et al. 808 nm driven Nd^{3+}-sensitized upconversion nanostructures for photodynamic therapy and simultaneous fluorescence imaging. Nanoscale. 2015; 7: 190-7.
5. Yue C, Liu P, Zheng M, Zhao P, Wang Y, Ma Y, et al. IR-780 dye loaded tumor targeting theranostic nanoparticles for NIR imaging and photothermal therapy. Biomaterials. 2013; 34: 6853-61.
6. Hildebrandt B, Wust P, Ahlers O, Dieing A, Sreenivasa G, Kerner T, et al. The cellular and molecular basis of hyperthermia. Crit Rev Oncol Hematol. 2002; 43: 33-56.
7. Rossi S, Di Stasi M, Buscarini E, Quaretti P, Garbagnati F, Squassante L, et al. Percutaneous RF interstitial thermal ablation in the treatment of hepatic cancer. AJR Am J Roentgenol. 1996; 167: 759-68.
8. Fujimoto S, Takahashi M, Mutou T, Kobayashi K, Toyosawa T. Successful intraperitoneal hyperthermic chemoperfusion for the prevention of postoperative peritoneal recurrence in patients with advanced gastric carcinoma. Cancer. 1999; 85: 529-34.
9. Pettigrew RT, Galt JM, Ludgate CM, Smith A. Clinical effects of whole-body hyperthermia in advanced malignancy. Br Med J. 1974; 4: 679-82.
10. Wust P, Hildebrandt B, Sreenivasa G, Rau B, Gellermann J, Riess H, et al. Hyperthermia in combined treatment of cancer. Lancet Oncol. 2002; 3: 487-97.
11. Sonvico F, Mornet S, Vasseur S, Dubernet C, Jaillard D, Degrouard J, et al. Folate-Conjugated Iron Oxide Nanoparticles for Solid Tumor Targeting as Potential Specific Magnetic Hyperthermia Mediators: Synthesis, Physicochemical Characterization, and in Vitro Experiments. Bioconjug Chem. 2005; 16: 1181-8.
12. Hayashi K, Ono K, Suzuki H, Sawada M, Moriya M, Sakamoto W, et al. High-Frequency, Magnetic-Field-Responsive Drug Release from Magnetic Nanoparticle/Organic Hybrid Based on Hyperthermic Effect. ACS Appl Mater Interfaces. 2010; 2: 1903-11.
13. Weissleder R. A clearer vision for in vivo imaging. Nat Biotech. 2001; 19: 316-7.
14. Huang X, El-Sayed IH, Qian W, El-Sayed MA. Cancer Cell Imaging and Photothermal Therapy in the Near-Infrared Region by Using Gold Nanorods. J Am Chem Soc. 2006; 128: 2115-20.
15. Dickerson EB, Dreaden EC, Huang X, El-Sayed IH, Chu H, Pushpanketh S, et al. Gold nanorod assisted near-infrared plasmonic photothermal therapy (PPTT) of squamous cell carcinoma in mice. Cancer Lett. 2008; 269: 57-66.
16. El-Sayed IH, Huang X, El-Sayed MA. Selective laser photo-thermal therapy of epithelial carcinoma using anti-EGFR antibody conjugated gold nanoparticles. Cancer Lett. 2006; 239: 129-35.
17. Yang K, Hu L, Ma X, Ye S, Cheng L, Shi X, et al. Multimodal imaging guided photothermal therapy using functionalized graphene nanosheets anchored with magnetic nanoparticles. Adv Mater. 2012; 24: 1868-72.
18. Zha Z, Yue X, Ren Q, Dai Z. Uniform polypyrrole nanoparticles with high photothermal conversion efficiency for photothermal ablation of cancer cells. Adv Mater. 2013; 25: 777-82.
19. Moon HK, Lee SH, Choi HC. In Vivo Near-Infrared Mediated Tumor Destruction by Photothermal Effect of Carbon Nanotubes. ACS Nano. 2009; 3: 3707-13.
20. Liu X, Tao H, Yang K, Zhang S, Lee S-T, Liu Z. Optimization of surface chemistry on single-walled carbon nanotubes for in vivo photothermal ablation of tumors. Biomaterials. 2011; 32: 144-51.
21. Yang K, Zhang S, Zhang G, Sun X, Lee S-T, Liu Z. Graphene in mice: ultrahigh in vivo tumor uptake and efficient photothermal therapy. Nano Lett. 2010; 10: 3318-23.
22. Robinson JT, Tabakman SM, Liang Y, Wang H, Sanchez Casalongue H, Vinh D, et al. Ultrasmall reduced graphene oxide with high near-infrared absorbance for photothermal therapy. J Am Chem Soc. 2011; 133: 6825-31.
23. Zhou M, Zhang R, Huang M, Lu W, Song S, Melancon MP, et al. A Chelator-Free Multifunctional [^{64}Cu]CuS Nanoparticle Platform for Simultaneous Micro-PET/CT Imaging and Photothermal Ablation Therapy. J Am Chem Soc. 2010; 132: 15351-8.
24. Zhou M, Li J, Liang S, Sood AK, Liang D, Li C. CuS Nanodots with Ultrahigh Efficient Renal Clearance for Positron Emission Tomography Imaging and Image-Guided Photothermal Therapy. ACS Nano. 2015; 9: 7085-96.
25. Chen WR, Adams RL, Higgins AK, Bartels KE, Nordquist RE. Photothermal effects on murine mammary tumors using indocyanine green and an 808-nm diode laser: an in vivo efficacy study. Cancer Lett. 1996; 98: 169-73.
26. Zheng X, Xing D, Zhou F, Wu B, Chen WR. Indocyanine Green-Containing Nanostructure as Near Infrared Dual-Functional Targeting Probes for Optical Imaging and Photothermal Therapy. Mol Pharm. 2011; 8: 447-56.
27. Yuan A, Wu J, Tang X, Zhao L, Xu F, Hu Y. Application of near-infrared dyes for tumor imaging, photothermal, and photodynamic therapies. J Pharm Sci. 2013; 102: 6-28.
28. Huang P, Bao L, Zhang C, Lin J, Luo T, Yang D, et al. Folic acid-conjugated silica-modified gold nanorods for X-ray/CT imaging-guided dual-mode radiation and photo-thermal therapy. Biomaterials. 2011; 32: 9796-809.
29. Kim J, Park S, Lee JE, Jin SM, Lee JH, Lee IS, et al. Designed fabrication of multifunctional magnetic gold nanoshells and their application to magnetic resonance imaging and photothermal therapy. Angew Chem. 2006; 118: 7918-22.
30. Zhou Z, Sun Y, Shen J, Wei J, Yu C, Kong B, et al. Iron/iron oxide core/shell nanoparticles for magnetic targeting MRI and near-infrared photothermal therapy. Biomaterials. 2014; 35: 7470-8.
31. Liang X, Li Y, Li X, Jing L, Deng Z, Yue X, et al. PEGylated Polypyrrole Nanoparticles Conjugating Gadolinium Chelates for Dual-Modal MRI/Photoacoustic Imaging Guided Photothermal Therapy of Cancer. Adv Funct Mater. 2015; 25: 1451-62.
32. Shang W, Zeng C, Du Y, Hui H, Liang X, Chi C, et al. Core–Shell Gold Nanorod@Metal–Organic Framework Nanoprobes for Multimodality Diagnosis of Glioma. Adv Mater. 2017; 29: 1604381.
33. Jang B, Park S, Kang SH, Kim JK, Kim S-K, Kim I-H, et al. Gold nanorods for target selective SPECT/CT imaging and photothermal therapy in vivo. Quant Imaging Med Surg. 2012; 2: 1.
34. Ntziachristos V. Going deeper than microscopy: the optical imaging frontier in biology. Nat methods. 2010; 7: 603-14.
35. Monici M. Cell and tissue autofluorescence research and diagnostic applications. Biotechnol Annu Rev. 2005; 11: 227-56.
36. Hilderbrand SA, Weissleder R. Near-infrared fluorescence: application to in vivo molecular imaging. Curr Opin Chem Biol. 2010; 14: 71-9.
37. Liu T-Y, Lo C-L, Huang C-C, Lin S-L, Chang CA. Engineering Nanomaterials for Biosensors and Therapeutics. In: Cai W, editor. Engineering in translational medicine. London: Springer; 2014.
38. Chatterjee DK, Fong LS, Zhang Y. Nanoparticles in photodynamic therapy: an emerging paradigm. Adv Drug Deliv Rev. 2008; 60: 1627-37.
39. Cui S, Yin D, Chen Y, Di Y, Chen H, Ma Y, et al. In Vivo Targeted Deep-Tissue Photodynamic Therapy Based on Near-Infrared Light Triggered Upconversion Nanoconstruct. ACS Nano. 2013; 7: 676-88.
40. Shen J, Zhao L, Han G. Lanthanide-doped upconverting luminescent nanoparticle platforms for optical imaging-guided drug delivery and therapy. Adv Drug Deliv Rev. 2013; 65: 744-55.
41. Wang Y, Shen P, Li C, Wang Y, Liu Z. Upconversion fluorescence resonance energy transfer based biosensor for ultrasensitive detection of matrix metalloproteinase-2 in blood. Anal Chem. 2012; 84: 1466-73.
42. Li Y, Tang J, He L, Liu Y, Liu Y, Chen C, et al. Core–Shell Upconversion Nanoparticle@Metal–Organic Framework Nanoprobes for Luminescent/Magnetic Dual-Mode Targeted Imaging. Adv Mater. 2015; 27: 4075-80.
43. Chatterjee DK, Rufaihah AJ, Zhang Y. Upconversion fluorescence imaging of cells and small animals using lanthanide doped nanocrystals. Biomaterials. 2008; 29: 937-43.
44. Hilderbrand SA, Shao F, Salthouse C, Mahmood U, Weissleder R. Upconverting luminescent nanomaterials: application to in vivo bioimaging. Chem Commun. 2009; 0: 4188-90.
45. Shan G, Weissleder R, Hilderbrand SA. Upconverting organic dye doped core-shell nano-composites for dual-modality NIR imaging and photo-thermal therapy. Theranostics. 2013; 3: 267-74.
46. Chen Q, Wang C, Cheng L, He W, Cheng Z, Liu Z. Protein modified upconversion nanoparticles for imaging-guided combined photothermal and photodynamic therapy. Biomaterials. 2014; 35: 2915-23.

47. Robinson JT, Welsher K, Tabakman SM, Sherlock SP, Wang H, Luong R, et al. High performance in vivo near-IR (>1 μm) imaging and photothermal cancer therapy with carbon nanotubes. Nano Res. 2010; 3: 779-93.
48. Jang B, Park J-Y, Tung C-H, Kim I-H, Choi Y. Gold Nanorod−Photosensitizer Complex for Near-Infrared Fluorescence Imaging and Photodynamic/Photothermal Therapy In Vivo. ACS Nano. 2011; 5: 1086-94.
49. Liu X, Que I, Kong X, Zhang Y, Tu L, Chang Y, et al. In vivo 808 nm image-guided photodynamic therapy based on an upconversion theranostic nanoplatform. Nanoscale. 2015; 7: 14914-23.
50. Li Y, Tang J, Pan D-X, Sun L-D, Chen C, Liu Y, et al. A Versatile Imaging and Therapeutic Platform Based on Dual-Band Luminescent Lanthanide Nanoparticles toward Tumor Metastasis Inhibition. ACS Nano. 2016; 10: 2766-73.
51. Ding X, Liu J, Liu D, Li J, Wang F, Li L, et al. Multifunctional core/satellite polydopamine@Nd^{3+}-sensitized upconversion nanocomposite: A single 808 nm near-infrared light-triggered theranostic platform for in vivo imaging-guided photothermal therapy. Nano Res. 2017; 10: 3434-46.
52. Sun Q, You Q, Pang X, Tan X, Wang J, Liu L, et al. A photoresponsive and rod-shape nanocarrier: Single wavelength of light triggered photothermal and photodynamic therapy based on AuNRs-capped & Ce6-doped mesoporous silica nanorods. Biomaterials. 2017; 122: 188-200.
53. Liu B, Li C, Yang P, Hou Z, Lin J. 808-nm-Light-Excited Lanthanide-Doped Nanoparticles: Rational Design, Luminescence Control and Theranostic Applications. Adv Mater. 2017; 29: 1605434.
54. Shen J, Chen G, Vu A-M, Fan W, Bilsel OS, Chang C-C, et al. Engineering the Upconversion Nanoparticle Excitation Wavelength: Cascade Sensitization of Tri-doped Upconversion Colloidal Nanoparticles at 800 nm. Adv Opt Mater. 2013; 1: 644-50.
55. Zhong Y, Tian G, Gu Z, Yang Y, Gu L, Zhao Y, et al. Elimination of photon quenching by a transition layer to fabricate a quenching-shield sandwich structure for 800 nm excited upconversion luminescence of Nd^{3+}-sensitized nanoparticles. Adv Mater. 2014; 26: 2831-7.
56. Zou W, Visser C, Maduro JA, Pshenichnikov MS, Hummelen JC. Broadband dye-sensitized upconversion of near-infrared light. Nat Photonics. 2012; 6: 560-4.
57. Xie X, Gao N, Deng R, Sun Q, Xu Q-H, Liu X. Mechanistic investigation of photon upconversion in Nd^{3+}-sensitized core–shell nanoparticles. J Am Chem Soc. 2013; 135: 12608-11.
58. Wang Y-F, Liu G-Y, Sun L-D, Xiao J-W, Zhou J-C, Yan C-H. Nd^{3+}-sensitized upconversion nanophosphors: efficient in vivo bioimaging probes with minimized heating effect. ACS Nano. 2013; 7: 7200-6.
59. Lu F, Yang L, Ding Y, Zhu JJ. Highly Emissive Nd^{3+}-Sensitized Multilayered Upconversion Nanoparticles for Efficient 795 nm Operated Photodynamic Therapy. Adv Funct Mater. 2016.
60. Hsu C-C, Lin S-L, Chang CA. Lanthanide-Doped Core–Shell–Shell Nanocomposite for Dual Photodynamic Therapy and Luminescence Imaging by a Single X-ray Excitation Source. ACS Appl Mater Interfaces. 2018; 10: 7859-70.
61. Liu K, Liu X, Zeng Q, Zhang Y, Tu L, Liu T, et al. Covalently Assembled NIR Nanoplatform for Simultaneous Fluorescence Imaging and Photodynamic Therapy of Cancer Cells. ACS Nano. 2012; 6: 4054-62.
62. Roper DK, Ahn W, Hoepfner M. Microscale Heat Transfer Transduced by Surface Plasmon Resonant Gold Nanoparticles. J Phys Chem C. 2007; 111: 3636-41.
63. Tian Q, Jiang F, Zou R, Liu Q, Chen Z, Zhu M, et al. Hydrophilic Cu9S5 Nanocrystals: A Photothermal Agent with a 25.7% Heat Conversion Efficiency for Photothermal Ablation of Cancer Cells in Vivo. ACS Nano. 2011; 5: 9761-71.
64. Zhang F. Near-infrared Nanomaterials: Preparation, Bioimaging and Therapy Applications. In: Zhang F, editor. Photon Upconversion Nanomaterials. Berlin: Springer-Verlag. 2016: 187-226.
65. Chen Y, Liu B, Deng X, Huang S, Hou Z, Li C, et al. Multifunctional Nd^{3+}-sensitized upconversion nanomaterials for synchronous tumor diagnosis and treatment. Nanoscale. 2015; 7: 8574-83.
66. Liu J, Zhang T, Song X, Xing J. Enhanced red emission of 808 nm excited upconversion nanoparticles by optimizing the composition of shell for efficient generation of singlet oxygen. Opt Mater. 2018; 75: 79-87.
67. Liu D, Xu X, Du Y, Qin X, Zhang Y, Ma C, et al. Three-dimensional controlled growth of monodisperse sub-50 nm heterogeneous nanocrystals. Nat Commun. 2016; 7: 10254.
68. Qian H-S, Zhang Y. Synthesis of Hexagonal-Phase Core−Shell NaYF4 Nanocrystals with Tunable Upconversion Fluorescence. Langmuir. 2008; 24: 12123-5.
69. Bootz A, Vogel V, Schubert D, Kreuter J. Comparison of scanning electron microscopy, dynamic light scattering and analytical ultracentrifugation for the sizing of poly (butyl cyanoacrylate) nanoparticles. Eur J Pharm Biopharm. 2004; 57: 369-75.
70. Dieckmann Y, Cölfen H, Hofmann H, Petri-Fink A. Particle size distribution measurements of manganese-doped ZnS nanoparticles. Anal Chem. 2009; 81: 3889-95.
71. Fissan H, Ristig S, Kaminski H, Asbach C, Epple M. Comparison of different characterization methods for nanoparticle dispersions before and after aerosolization. Anal Methods. 2014; 6: 7324-34.
72. Zhang C, Lee JY. Prevalence of Anisotropic Shell Growth in Rare Earth Core–Shell Upconversion Nanocrystals. ACS Nano. 2013; 7: 4393-402.
73. Chen C, Kang N, Xu T, Wang D, Ren L, Guo X. Core–shell hybrid upconversion nanoparticles carrying stable nitroxide radicals as potential multifunctional nanoprobes for upconversion luminescence and magnetic resonance dual-modality imaging. Nanoscale. 2015; 7: 5249-61.
74. Dong H, Sun L-D, Wang Y-F, Xiao J-W, Tu D, Chen X, et al. Photon upconversion in Yb^{3+}–Tb^{3+} and Yb^{3+}–Eu^{3+} activated core/shell nanoparticles with dual-band excitation. J Mater Chem C. 2016; 4: 4186-92.
75. Liu J-N, Bu W-B, Shi J-L. Silica coated upconversion nanoparticles: A versatile platform for the development of efficient theranostics. Acc Chem Res. 2015; 48: 1797-805.
76. Idris NM, Gnanasammandhan MK, Zhang J, Ho PC, Mahendran R, Zhang Y. In vivo photodynamic therapy using upconversion nanoparticles as remote-controlled nanotransducers. Nat Med. 2012; 18: 1580-5.
77. Liu J, Bu W, Pan L, Shi J. NIR-Triggered Anticancer Drug Delivery by Upconverting Nanoparticles with Integrated Azobenzene-Modified Mesoporous Silica. Angew Chem Int Ed. 2013; 52: 4375-9.
78. Chen Y, Chen H, Shi J. In Vivo Bio-Safety Evaluations and Diagnostic/Therapeutic Applications of Chemically Designed Mesoporous Silica Nanoparticles. Adv Mater. 2013; 25: 3144-76.
79. Janeesh P, Sami H, Dhanya C, Sivakumar S, Abraham A. Biocompatibility and genotoxicity studies of polyallylamine hydrochloride nanocapsules in rats. RSC Adv. 2014; 4: 24484-97.
80. Li HL, He YX, Gao QH, Wu GZ. Folate-polyethylene glycol conjugated carboxymethyl chitosan for tumor-targeted delivery of 5-fluorouracil. Mol Med Rep. 2014; 9: 786-92.
81. Niidome T, Yamagata M, Okamoto Y, Akiyama Y, Takahashi H, Kawano T, et al. PEG-modified gold nanorods with a stealth character for in vivo applications. J Control Release. 2006; 114: 343-7.
82. Ow H, Larson DR, Srivastava M, Baird BA, Webb WW, Wiesner U. Bright and stable core− shell fluorescent silica nanoparticles. Nano Lett. 2005; 5: 113-7.
83. Lin S-L, Liu T-Y, Lo C-L, Wang B-S, Lee Y-J, Lin K-Y, et al. Synthesis, surface modification, and photophysical studies of Ln_2O_2S:Ln^{3+}(Ln= Gd, Tb, Eu; Ln′= Tb and/or Eu) nanoparticles for luminescence bioimaging. J Lumin. 2016; 175: 165-75.
84. Chen G, Damasco J, Qiu H, Shao W, Ohulchanskyy TY, Valiev RR, et al. Energy-cascaded upconversion in an organic dye-sensitized core/shell fluoride nanocrystal. Nano Lett. 2015; 15: 7400-7.
85. Shao Q, Li X, Hua P, Zhang G, Dong Y, Jiang J. Enhancing the upconversion luminescence and photothermal conversion properties of~ 800nm excitable core/shell nanoparticles by dye molecule sensitization. J Colloid Interface Sci. 2017; 486: 121-7.
86. Wu X, Zhang Y, Takle K, Bilsel O, Li Z, Lee H, et al. Dye-sensitized core/active shell upconversion nanoparticles for optogenetics and bioimaging applications. ACS Nano. 2016; 10: 1060-6.
87. Fischer S, Bronstein ND, Swabeck JK, Chan EM, Alivisatos AP. Precise tuning of surface quenching for luminescence enhancement in core–shell lanthanide-doped nanocrystals. Nano Lett. 2016; 16: 7241-7.
88. Li Y, Zhang J, Zhang X, Luo Y, Ren X, Zhao H, et al. Near-Infrared to Visible Upconversion in Er^{3+} and Yb^{3+} Codoped Lu_2O_3 Nanocrystals: Enhanced Red Color Upconversion and Three-Photon Process in Green Color Upconversion. J Phys Chem C. 2009; 113: 4413-8.
89. Wang Y, Tu L, Zhao J, Sun Y, Kong X, Zhang H. Upconversion Luminescence of β-$NaYF_4$:Yb^{3+}, Er^{3+}@β-$NaYF_4$ Core/Shell Nanoparticles: Excitation Power Density and Surface Dependence. J Phys Chem C. 2009; 113: 7164-9.
90. Chen G, Qiu H, Prasad PN, Chen X. Upconversion nanoparticles: design, nanochemistry, and applications in theranostics. Chem Rev. 2014; 114: 5161-214.
91. Zheng M, Zhao P, Luo Z, Gong P, Zheng C, Zhang P, et al. Robust ICG Theranostic Nanoparticles for Folate Targeted Cancer Imaging and Highly Effective Photothermal Therapy. ACS Appl Mater Interfaces. 2014; 6: 6709-16.
92. Li S, Zhou S, Li Y, Li X, Zhu J, Fan L, et al. Exceptionally High Payload of the IR780 Iodide on Folic Acid-Functionalized Graphene Quantum Dots for Targeted Photothermal Therapy. ACS Appl Mater Interfaces. 2017; 9: 22332-41.
93. Zeng S, Tsang M-K, Chan C-F, Wong K-L, Hao J. PEG modified BaGdF5: Yb/Er nanoprobes for multi-modal upconversion fluorescent, in vivo X-ray computed tomography and biomagnetic imaging. Biomaterials. 2012; 33: 9232-8.